Indian Journal of Pure & Applied Physics
Vol. 61, April 2023, pp. 258-267
DOI: 10.56042/ijpap.v61i4.70872

Fabricating FeCrCoZrLa High Entropy Alloy towards Enhanced Photocatalytic Degradation of Methylene Blue Dye

Hakan Yaykaşlı

Kahramanmaras İstiklal University, Elbistan Vocational School of Higher Education, Kahramanmaraş, Turkey

Received 25 January 2023; accepted 28 March 2023

$Fe_{20}Cr_{20}Co_{20}Zr_{20}La_{20}$ (at. %) high entropy alloy (HEA) using mechanical alloy (MA) was synthesized by an equiatomic ratio as a function of milling times (0h, 5h, 10h, 20h, 30h, and 50h). The HEA alloys were characterized with X-ray diffractometer (XRD), scanning electron microscopy (SEM), X-ray Energy-Dispersive Spectroscopy (EDX), transmission electron microscopy (TEM), and Differential thermal analysis (DTA). After 50 hours of grinding, the BCC crystalline phase was formed and the crystallite size and microstrain were calculated at 4.7 nm and 1.95 nm, respectively. TEM image of 50 hours of milled powders also confirms a nanocrystalline structure. Using solar energy, visible light photocatalysis is a promising method for removing environmental pollution. The photocatalytic effect of the synthesized nanostructured alloy on aqueous solutions containing methylene blue (MB) was investigated under xenon light. Photocatalytic degradation of the synthesized sample was evaluated by calculating the absorbance drops of the UV–Vis absorption spectra (methylene blue 664 nm).The degradation of the nanostructured alloy for MB was found as 89.76% after 120 min. This implies that the photocatalytic degradation rate is relatively high, and the obtained alloy has been used in practice for the degradation of methylene blue dye effectively.

Keywords: FeCrCoZrLa High-entropy alloys; Mechanical alloying; Photocatalytic properties; Methylene blue

1 Introduction

High entropy alloys (HEA) were firstly described in 2004. HEA is an alloy formed by combining at least five elements at 5% and 35% ratios[1]. High entropy alloys have remarkable advantages over conventional alloys with their superior properties, lattice distortion effect, slow diffusion effect, high entropy effect, and cocktail effect[2]. In addition, HEA does not contain complex intermetallic compounds[3]. Besides, the formation of simple solid solution phases such as face-centered cubic (FCC) and body-centered cubic (BCC), and hexagonal closed package (HCP) in HEA due to high mixing entropy has been reported in the literature[4]. HEAs are potential candidates for structural applications especially in refractory materials as they can operate at high temperatures[5]. Moreover, they have increased strength, hardness, wear resistance, corrosion resistance, oxidation resistance, and stability at high temperatures[6,7]. HEAs can be produced using mechanical alloying (MA), electron beam melting, and arc melting[8]. The mechanical alloying method has advantages such as obtaining nanocrystalline, homogeneous, or amorphous alloys[9,10]. In the MA technique, alloying parameters such as grinding time, grinding speed, ball/powder ratio, and process control agent affect the microstructure and phase development of the powders, and the production can be easily controlled[11]. Moreover, this superior technique allows using elements with different melting temperatures to synthesize alloys[12].

The synthesis and applications of high entropy alloys with transition metals systems are examined in literature[13–15] but there are few studies related to rare earth elements' high entropy alloys (RHEA)[16,17]. For instance, the addition of RE elements Y or Ce to austenitic steel is known to increase high-temperature oxidation resistance and provide good fracture toughness in alloys such as magnesium, titanium, and cobalt-chromium[18]. In recent years, one of the most studied alloy composition in the HEA has been CoCrFeNi, and for instance CoCrFeNi-Mo[19], CoCrFeNi-Al [20], CoCrFeNi-Nb[21], CoCrFeNi-Mn[22], CoCrFeNi-Y_2O_3[23]. It is known that the use of rare earth elements in HEA has positive effects on the microstructure[24]. Wang *et al*. showed that Nd added in CoCrFeMnNi HEAs could induce precipitates, resulting in solid solution reinforcement, grain refinement, and precipitation enhancement[25]. It has

Corresponding author:
(E-mail: hakan.yaykasli@istiklal.edu.tr)

been reported that adding elements to CoCrFeNi HEAs has effects such as grain refinement, solid solution, and precipitation strengthening[19]. A few studies investigate the impact of RE elements on the microstructure and thermal and mechanical properties by adding them to HEAs[16,18,26]. Li *et al*. studied the $FeCoNi_{1.5}CuBY_{0.2}$ HEAs and improved the alloy's mechanical properties due to the dispersion strengthening of the YB6 precipitates[27]. Although the CrMnFeNi alloy has been investigated, it is expected that the functional properties desired from these alloys will be improved[28].

Studies related to HEAs generally focus on mechanical, oxidation, and corrosion and thermal properties. The photocatalytic performance of this novel alloy system have been are rarely investigated[29–31]. Waste dye materials are one of the significant factors that negatively affecting health of human and other living organism[32]. Therefore, the treatment of waste dye material is critical. Various methods are used to remove waste dye materials, including different physical and chemical processes. Among these techniques, processes such as photocatalytic oxidation are kinetically accelerated, which is of interest to researchers[33]. Lv *et al*. reported that an AlCoCrTiZn HEA synthesized with MA showed a significant capacity for the degradation of the azo dye Direct Blue 6 (DB6)[28]. Petrovic *et al*. reported that a ball milling process synthesized LaTiMgFeO perovskite. The photocatalytic activity of perovskite was studied by photo degradation of methyl orange and methylene blue dyes under UV light irradiation. The LaTiMgFe sample exhibited, after 180 min irradiation, the highest photo degradation activity towards an MB with a conversion of 63%[34]. It aims to develop a new HEA for the degradation of dye materials.

In this study, nanocrystalline FeCrCoZrLa high entropy alloy containing rare earth element is synthesized by a mechanical alloying technique. The microstructure and crystal structure properties of the FeCrCoZrLa alloy were analyzed by scanning electron microscopy (SEM), X-ray diffraction (XRD), and transmission electron microscopy (TEM). In addition, element mapping and phase distribution were performed using energy dispersive spectroscopy (EDS). The effect of milling time on particle dissolution, microstructural evolution, and phase transformation have been investigated. The photocatalytic performance of the obtained powder alloy has been examined. The degradation capacity of FeCrCoZrLa alloy to decompose methylene blue solution has been measured.

2 Experimental

2.1 Synthesis of the $Fe_{20}Cr_{20}Co_{20}Zr_{20}La_{20}$ HEA

$Fe_{20}Cr_{20}Co_{20}Zr_{20}La_{20}$ (at. %) high entropy alloy using mechanical alloy (MA), iron(Fe), chromium (Cr), cobalt (Co), zirconium (Zr), and lanthanum (La), and powders starting elements with a purity higher than 99.9% by weight and particle size less than 45 µm were synthesized by equiatomic ratio. Starting components used in the synthesis have been purchased from Alfa Aesar and Merck. In the milling process were used stainless steel vials and stainless-steel grinding balls of different sizes were used as a process controlling agent (0.1% methanol). HEAs were milled in a high-energy planetary ball mill (Fritsch Pulverisette 5) at a ball-to-powder weight ratio of 20:1 with a 300-rpm rotation speed. During the grinding process, to prevent the vials from overheating, the milling machine was set to run for 20 minutes and stop for 20 minutes. The HEAs powders were milled for up to 0h, 5h, 10h, 20h, 30h, and 50 hours. For characterization, the synthesis process was interrupted at specific intervals to extract the appropriate amount of milled HEAs. Fe, Cr, Co, Zr, and La powders of the physical, chemical, and mechanical properties are given in Table 1.

2.2 Characterization Techniques

The phase analysis of the HEA alloys was carried out employing an X-ray diffractometer (Philips X'Pert PRO) with CuK_α (λ = 1.54 A°) radiation 40 kV, 30 mA. The scan patterns were performed in

Table 1 — Characteristic properties of the elements

Element	Atomic Radius (ppm)	Melting Point (°C)	ρ (293K) (g/cm^3)	K(GPa)	n_{ws}
Iron	125	1535	7.87	170	1.77
Chromium	127	1857	7.19	160	1.73
Cobalt	126	1495	8.90	180	1.75
Zirconium	148	1852	6.51	NA	1.39
Lanthanum	169	920	6.15	28	1.09

n_{ws}:Electron density, K: Bulk modulus, ρ: Denstiy

the spectrum 2θ=20°-90°. The morphological microstructure of HEAs powders was investigated with scanning electron microscopy (SEM, ZEISS EVO LS10), X-ray Energy-Dispersive Spectroscopy (EDS), and transmission electron microscopy (TEM, Hitachi HighTech HT7700). HEA powder's thermal properties have characterizeda rate of 400 to 1000 °C at a heating rate of 10 °C/min through Differential thermal analysis (DTA, Perkin-Elmer Sapphire). UV–Vis absorption spectra of the 50h milled HEA powder was examined using a Shimadzu UV–Vis 1800 spectrometer in the 450–900 nm wavelength range.

The average crystallite size (D) of milled HEAs powders depending upon milling times was estimated using Scherrer's equation Eq. (1).

$$D = \frac{K\lambda}{\beta_{hkl}\cos\theta} \quad \ldots (1)$$

Here K is the shape factor with the value 0.90, λ demonstrates the X-ray wavelength, β_{hkl}, and cosθ is the full width at half maximum in radians and Bragg angle, respectively. Since the exact K-value is unknown for the present system, D-values are only estimates. The microstrain was determined by using the following Equation Eq. (2).

$$\varepsilon = \frac{\beta_{hkl}}{4\tan\theta} \quad \ldots (2)$$

2.3 Photocatalytic Degradation Experiments

UV-Vis spectroscopy was used to investigate the performance of the alloy in MB degradation. A 300W xenon lamp was chosen as the light source. MB solutions were prepared as 5 ppm (mg L^{-1}) for degradation measurements. 10 mg of alloy sample was mixed into 50 ml of MB solution. It was kept in the darkroom for 30 minutes, taking into account the adsorption-desorption balance. A sample of 2 mL was taken from the MB solution every 10 minutes, and after centrifugation, measurements were taken between 450-800 nm wavelengths. In addition, the decomposition of MB solution in room light and under xenon lamp without the addition of catalyst will be referred to as RL and XL. Then, 2 ml samples were taken every 10 minutes from 0 to 120 minutes, and their measurements were taken by scanning in UV-Vis spectroscopy.

2.4 Photocatalytic Degradation Characterization

The degradation efficiency of the nanostructured alloy produced in the study was calculated with the following Eq. (3).

$$Degradation(\%) = \left[1 - \frac{c_t}{c_0}\right] x100 \quad \ldots (3)$$

In the equation, C_0 is the initial concentration, and C_t is the concentration at the sampling time. The reaction kinetics of MB degradation was calculated according to the Langmuir-Hinshelwood (L-H) model. According to the L–H model, the Eq. (4) is as follows:

$$\ln\left(\frac{C_t}{C_0}\right) = k.t \quad \ldots (4)$$

In the equation: C_0 is the dye concentration at time zero, C_t is the dye concentration in the solution at time t, k is the rate constant, and t is the reaction time[32,35].

3 Results and Discussions

Using data from the Inorganic Crystal Structure Database (ICOD) and Crystallography Open Database (COD), the XRD patterns of the alloy's starting elements are given in Fig. 1. Fig. 1(a), peaks and miller indices were detected at 2θ angles at 44.69° (011), 65.09° (002), and 82.36° (112) in the XRD pattern of pure iron powder. Fig. 1(b), peaks and miller indices were detected in the XRD pattern of chrome powder at 2θ angles at 44.43° (110), 64.63° (220), 81.72° (211), and 91.19 (220). Fig. 1(c), peaks and miller indices were detected in the XRD pattern of cobalt powder at 2θ angles at 41.60° (100), 44.34° (002), 47.43° (101), 51.53° (002), and 75.93° (110). Fig. 1(d), zirconium powder in XRD pattern 32.12° (100), 35.08° (002), 36.75° (101), 44.56° (208), 48.17° (102), 57.15° (110), 63.78° (103), 68.72° (112), 69.76° (201), 73.77° (004), and 82.49° (104)

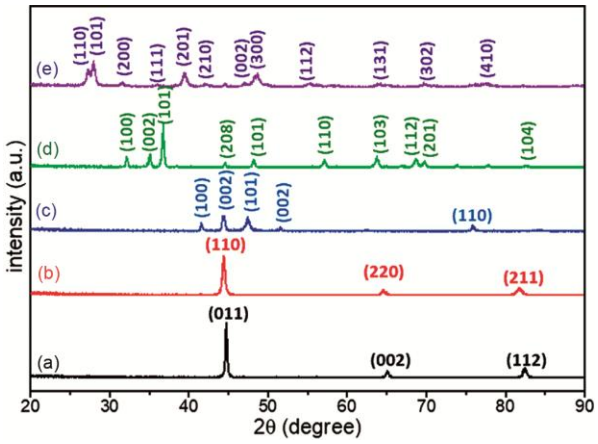

Fig. 1 — XRD pattern of starting materials (a) Fe, (b) Cr, (c) Co, (d) Zr and (e) La.

Table 2 — Crystallographic Parameters of starting materials

Element	Crystallographic Parameters					Reference Code
	Crystal System	Space Group	a(Å)	b(Å)	c(Å)	
Iron	Cubic	Im-3m	2.90	2.90	2.90	96-901-34788-(COD)
Chromium	Cubic	Im-3m	2.87	2.87	2.87	00-001-1261- (ICOD)
Cobalt	Hexagonal	P63/mmc	2.50	2.50	4.07	01-089-7094- (ICOD)
Zirconium	Hexagonal	P63/mmc	3.23	3.23	4.14	03-065-3366- (ICOD)
Lanthanum	Hexagonal	P63/mmc	6.54	6.54	3.85	01-083-2034- (ICOD)

Inorganic Crystal Structure Database (ICOD), Crystallography Open Database (COD)

peaks and miller indices at 2θ angles. Fig. 1(e), the XRD pattern of the lanthanum powder is 27.15° (110), 27.94° (101), 31.55° (200), 35.93° (111), 39.53° (201), 42.20° (210), 47.04° (002), 48.65° (300), 55.25° (112), 63.98° (131), 69.62° (302) and 77.63° (410) peaks at 2θ angles were detected. In addition, Table 2 are presented the crystallographic parameters of the starting elements.

The average valence electron concentration (VEC) is described by Eq. (5)

$$VEC = \sum_{i}^{n} c_i (VEC)_i \quad \ldots (5)$$

where, $(VEC)_i$ is the valance electron concentration of the i_{th} alloy element, c_i is the atomic percent i_{th} alloy element.VEC is a critical parameter for designing FCC if VEC>8, BCC if VEC<6.87, and FCC+BCC if VEC in between 6.87≤VEC<8.0,

The mixing enthalpy calculation of ΔH_{mix} is described by Eq. (6)[36,37].

$$\Delta H_{mix} = \sum_{i=1, i\neq j}^{n} \Omega_{ij} c_i c_j \ , \ \Omega_{ij} = 4\Delta H_{mix}^{Ab} \quad \ldots (6)$$

where $4\Delta H_{mix}^{Ab}$ is defined as the mixing enthalpy of binary A-B alloys in the liquid state, c_i and c_j are an atomic percentage of the i_{th} and j_{th} element, respectively; and using values from http://www.entall.imim.pl/calculator/ as by definition $H_{mix/ij}$ is taken for equimolar pairs.

The HEAs, the mixing entropy ΔS_{mix} is defined Eq.(7), and where R is the gas constant, 8.314 J $K^{-1}mol^{-1}$,

$$\Delta S_{mix} = -R\sum_{i=1}^{n} c_i \ln c_i \quad \ldots (7)$$

The atomic size difference (δ) is defined Eq.(8)[38,39],

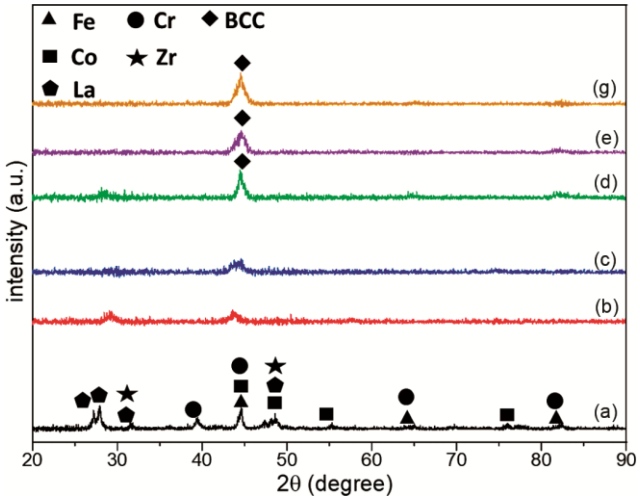

Fig. 2 — X-ray diffraction pattern of the $Fe_{20}Cr_{20}Co_{20}Zr_{20}La_{20}$ HEA synthesized by ball milled different times for: (a) 0h, (b) 5h, (c) 10h, (d) 20h, (e) 30h, and (f) 50h.

$$\delta = 100\sqrt{\sum_{i=1}^{n} c_i (1-\frac{r_i}{\bar{r}})^2} \ , \ \bar{r} = \sum_{i=1}^{n} c_i r_i \quad \ldots (8)$$

where r_i is the atomic radius of the i_{th} element, an amplifying factor 100 is used for ease of reading[40].

Figure 2 shows the milled XRD patterns of $Fe_{20}Cr_{20}Co_{20}Zr_{20}La_{20}$ HEA powders for different milling times (0h, 5h, 10h, 20h, 30h, and 50h). All metal powders were thoroughly mixed before grinding, and peaks of all pure elements (iron, chromium, cobalt, zirconium, and lanthanum) were analysed on the 0-hour Fig. 2(a) X-ray diffraction. It is observed that the XRD peaks of the starting powders disappeared after 5 hours of milling Fig. 2(b), and a decrease in the intensity of the La peak was observed. As the grinding time progressed (after 10 hours), all the XRD peaks Fig. 2(c) of the powders disappeared entirely and the simple crystal structure was formed. This crystal structure corresponds to the single-phase BCC structure. It known as the dissolution of the starting elements, and the formation of the solid solution is complete HEAs

Table 3 — Calculated thermodynamic- geometric parameters of HEA $Fe_{20}Cr_{20}Co_{20}Zr_{20}La_{20}$

Alloy	$\Delta H_{mix}\,(j/mol)$	$\Delta S_{mix}\,(J/mol.K)$	VEC	δ
$Fe_{20}Cr_{20}Co_{20}Zr_{20}La_{20}$	-10.97	13.38	6.6	2.84

in the BCC structure have been reported in the literature[20,41,42]. After 20, 30, and 50 hours of milling, the prominent diffraction peaks of the BCC crystal structure remained unchanged. Milling for 50 hours shows that the HEA alloy does not cause further changes in the XRD diffraction peaks. This indicates that the elements are perfectly mixed after 50 hours of grinding. The calculated VEC value of FeCrCoZrLa is 6.6 (Table 3) also confirms the formation of the BCC structure in HEA. It is commonly known that mechanical grinding leads to nanoparticle formation in materials due to severe plastic deformation and fracture[43]. Elements containing HEA alloy Fe, Co, Cr, Zr, and La have atomic radii of 126 pm, 128 pm, 125 pm, 160 pm, and 187 pm, respectively. Therefore, possible severe lattice distortion and solid solution formation are expected in HEAs. Crystallite sizes and micro strain were calculated using Scherrer's formula for all grinding times in the investigated FeCrCoZrLa HEA. The crystallite dimensions and micro-strain of the ground powder estimated by the Scherrer method are given in Fig. 3. After milling for 0, 5, 10, 20, 30, and 50 hours in FeCrCoZrLa HEA, the crystal sizes were calculated as 15.44 nm, 7.3 nm, 5.21 nm, 5.5 nm, 4.9 nm, and 4.7 nm, respectively. The crystal sizes of the alloys decreased continuously from 0 to 10 hours of the grinding time, while the crystal size remained almost stable at 20, 30, and 50 hours of grinding, indicating that the stability of the MA process was achieved. Micro-strain in FeCrCoZrLa HEA after milling at 0, 5, 10, 20, 30, and 50 hours was calculated as 1.18, 1.39, 1.67, 1.82, 1.86, and 1.95, respectively. As the milling time increases, the micro-strain increases, increasing the lattice stress. Therefore, the powder's crystal size reduction can be attributed to excessive refraction during the long-term MA process. The increased lattice strain is associated with size mismatch between the components, the high grain boundary fraction caused by crystallite refining, and increased dislocation density produced by severe plastic deformation during MA[13].

The good catalytic properties of nanostructured alloy materials are directly related to their morphological, crystalline sizes, and distributions[28]. SEM evaluated the microstructure and morphological evolution of the mechanically alloyed FeCrCoZrLa powder during milling. Fig. 4 presents SEM images

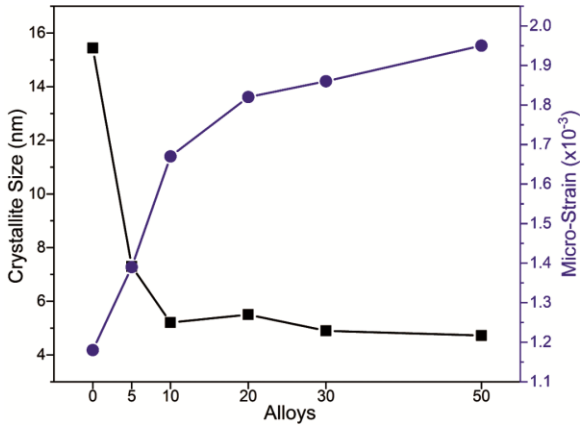

Fig. 3 — The average values of crystallite size (nm) and micro-strain of the $Fe_{20}Cr_{20}Co_{20}Zr_{20}La_{20}$ HEA synthesized by mechanical alloying for different milling durations.

of raw elemental powders of FeCrCoZrLa powder and powders ground at various times. Pure elemental powders were observed to have various morphologies. Average sizes of dust particles were determined from SEM micrographs using Image J software. The variation of powder particle sizes with milling time for ground powders is presented in Fig. 5. Before MA, the starting powders are characterized by granular particles with a size distribution of less than 17 μm. Furthermore, after extending the milling time to 10, 20, 30, and 50 hours, the particle size of the powder of the milled HEA FeCrCoZrLa changed drastically. After 5 hours (Fig. 4) of milling the mixed powders, the morphology shapes of Fe, Cr, Co, Zr, and La powders were changed, and the formation of a new microstructure with different surfaces, the particle size of which varies between 2 and 20 μm, was observed. It is well known that grinding mixed powders change the size of ball-milled powders thanks to crushing and cold welding[44,45]. In addition, it was observed that the particle size formed was between 5 and 10 μm by extending the grinding time up to 10 hours (Fig. 4). This is due to the assemblage of different starting components. This is mainly due to the adhesion of the mixed powders to the vial wall and the stainless-steel balls hardened by milling; the microstructure has turned into an inhomogeneous structure. These particles are exposed to cold welding, and spherical particles are formed milled for 10 hours (Fig. 4). The particle size is reduced to a

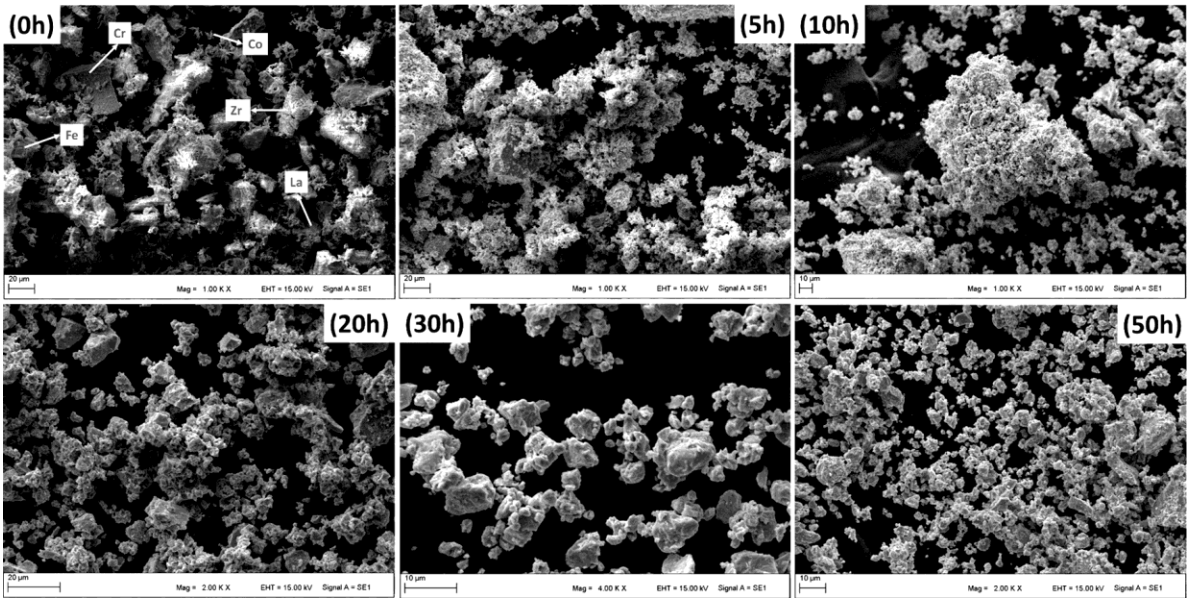

Fig. 4 — SEM micrographs of $Fe_{20}Cr_{20}Co_{20}Zr_{20}La_{20}$ HEA powders for various MA times.

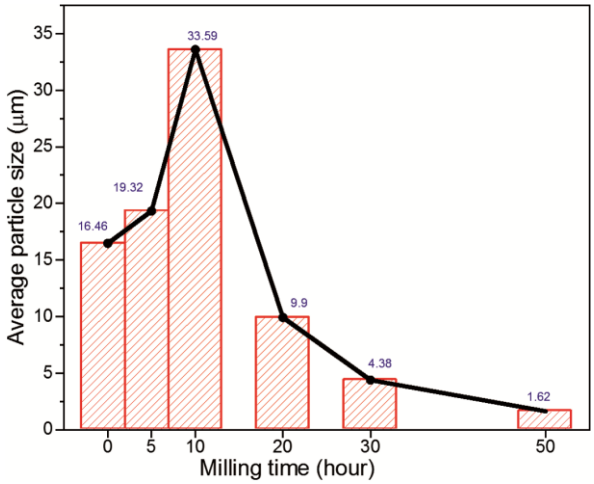

Fig. 5 — Average particle size for $Fe_{20}Cr_{20}Co_{20}Zr_{20}La_{20}$ HEA of various MA times.

homogeneous structure with 20 hours and 30 hours of milling time (Fig. 4). The increased grinding time, together with the increase in the density of defects caused by plastic deformation, leads to improved diffusion and, therefore alloy formation[43,46]. SEM image of milling time of 50 hours (Fig. 4), FeCrCoZrLa shows a homogeneous range of particle size distribution. The powder particles are typically in the form of spherical semi-agglomerates less than 1.6 µm in size.

Figures 6 & 7 present EDX mapping of $Fe_{20}Cr_{20}Co_{20}Zr_{20}La_{20}$ HEA powders milled at 0 and 50 hours, respectively. Fig. 6, distribution and morphology of Fe, Cr, Co, Zr, and La powders were determined by EDX mapping. These powders are of different shapes and dimensions. In the elements was not found oxidized structure. Fig. 7 shows that after 50 hours of milling, iron, chromium, cobalt, zirconium, and lanthanum are homogeneously dispersed, implying the solid solution phase. In addition, it was observed that the milling $Fe_{20}Cr_{20}Co_{20}Zr_{20}La_{20}$ alloy powders were not contaminated from any other elemental impurities, including oxygen.

TEM image of 50 hours milled $Fe_{20}Cr_{20}Co_{20}Zr_{20}La_{20}$ HEA is presented in Fig. 8. It confirms that $Fe_{20}Cr_{20}Co_{20}Zr_{20}La_{20}$ HEA powders is in a nanostructure. The obtained TEM micrographs indicate that the 50 h milled powders consist of agglomerates of small grains and spherical.

Figure 9 shows the DTA graph for $Fe_{20}Cr_{20}Co_{20}Zr_{20}La_{20}$ HEA for different milling times (0h, 5h, 10h, 20h, 30h and 50h). It can be clearly seen that HEAs are thermally stable between 400-1000 °C and there is no significant phase transformation in this range. In Fig. 9(a), there is an peak, which indicates the melting temperature of lanthanum, with a peak value of 920 °C of HEA at 0 hours. In addition, no endothermic peak was observed because the melting temperature of the other starting elements (Table 1) was above 1000 °C. In Fig. 9(b-f), no exothermic or endothermic was observed between 400 °C and 1000 °C in the DTA curve of 5h, 10h, 20h, 30h, and 50h milled HEA powders. This is associated with structural deformation and the release of internal stress caused by lattice strain[47].

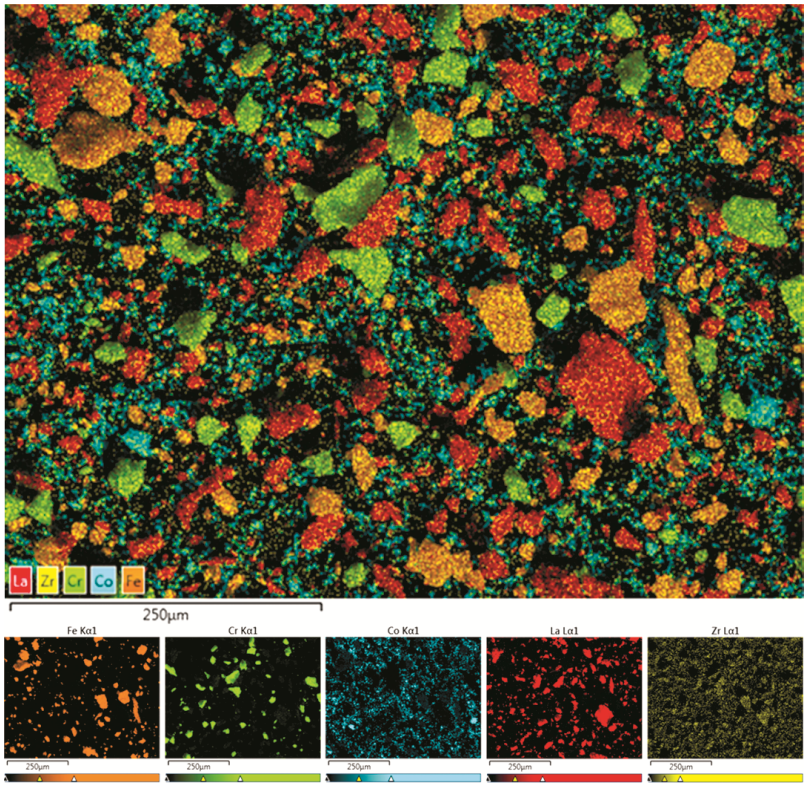

Fig.6 — EDX mapping result of $Fe_{20}Cr_{20}Co_{20}Zr_{20}La_{20}$ HEA powders for0 hour.

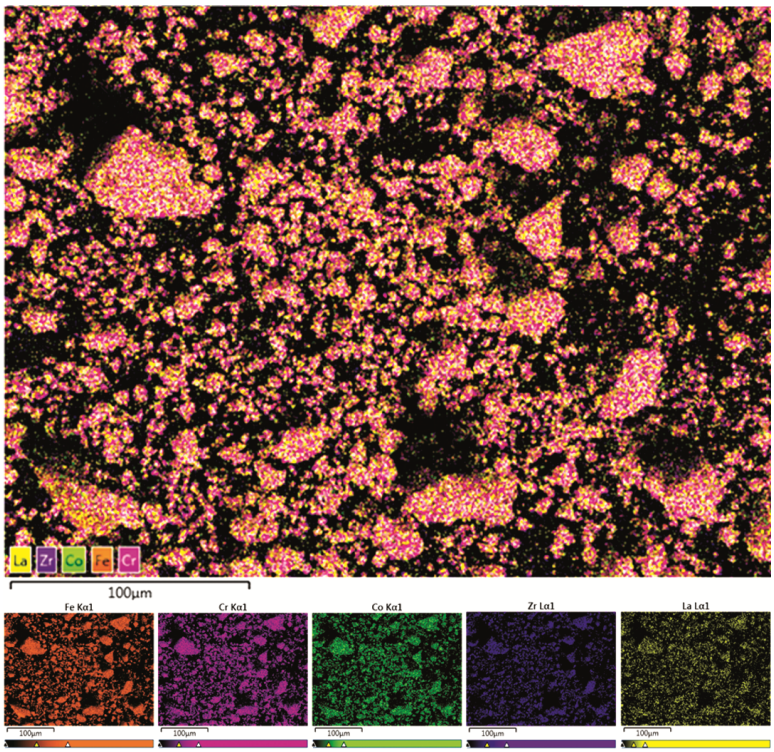

Fig. 7 — EDX mapping result of $Fe_{20}Cr_{20}Co_{20}Zr_{20}La_{20}$ HEA powders for 50 hours MA.

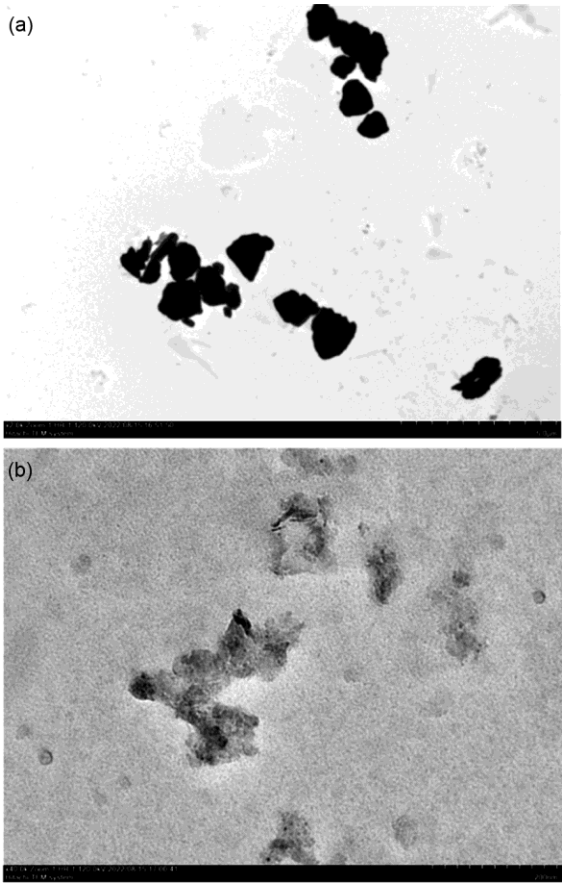

Fig. 8 — TEM micrographs of $Fe_{20}Cr_{20}Co_{20}Zr_{20}La_{20}$ HEA powders for 100h times.

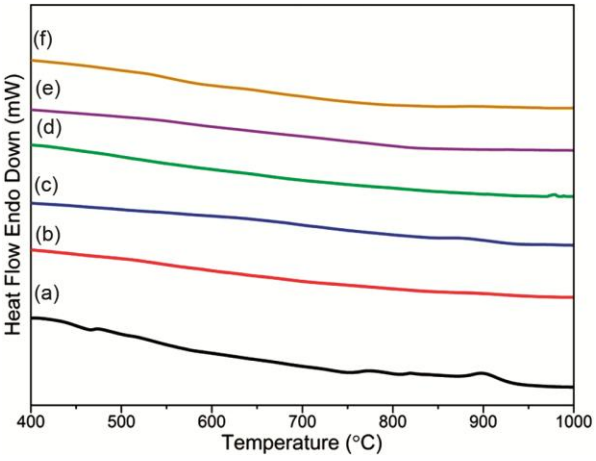

Fig. 9 — DTA curves of $Fe_{20}Cr_{20}Co_{20}Zr_{20}La_{20}$ HEA powders by ball milled different times for: (a) 0h, (b) 5h, (c) 10h, (d) 20h, (e) 30h, and (f) 50h.

Time-dependent photocatalytic degradation of methyl blue for nanostructured alloy was investigated under a solar simulator. Measurements were taken every 10 minutes for the alloy sample. Fig. 10 shows the absorbance graph for the MB solution under the

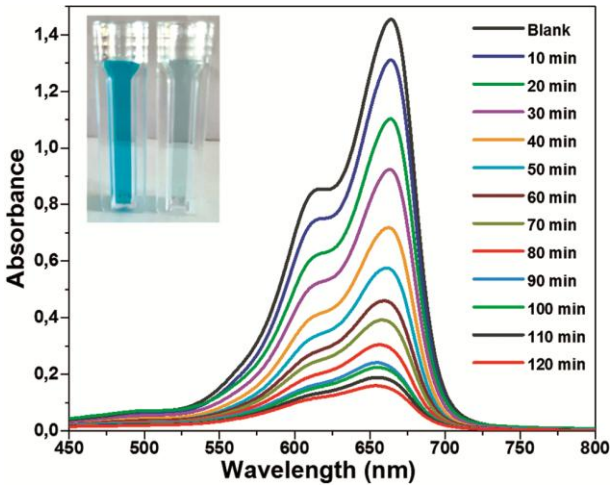

Fig. 10 — UV-visible absorption spectra for MB in the presence of nanostructure alloy.

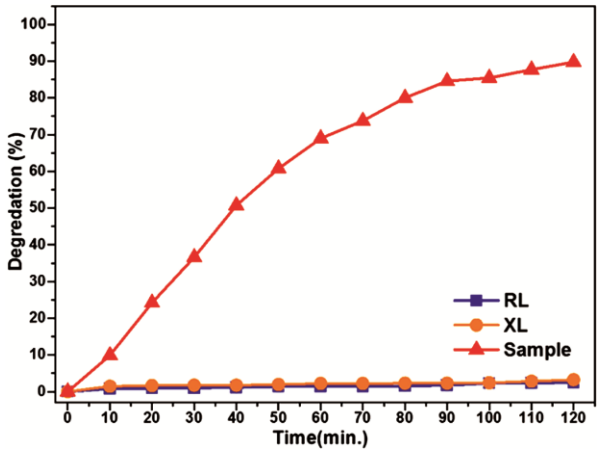

Fig. 11 — The photocatalytic degradation of MB the presence of alloy.

solar simulator. From the inset, MB solution becomes colorless after 120 min of degradation. As seen from this figure, the absorbance peak of sample decreases as a function of time.

In Fig. 11, the degradation rate of the nanostructured alloy sample in the MB dyestuff solution after 120 minutes is approximately 89.76%. Degradation rates of MB solutions without photocatalyst were found to be 2.47% and 3.23% in room light (RL) and solar simulator light (XL), respectively. This imply that the synthesized $Fe_{20}Cr_{20}Co_{20}Zr_{20}La_{20}$ rare earth element containing high entropy alloy is highly efficient catalyst for degradation of methylene blue dye. This is also important result related to photocatalytic performance of rare earth element containing high entropy alloys.

The photocatalytic degradation kinetic plot for the solution of MB is given in Fig. 12. The constant rate

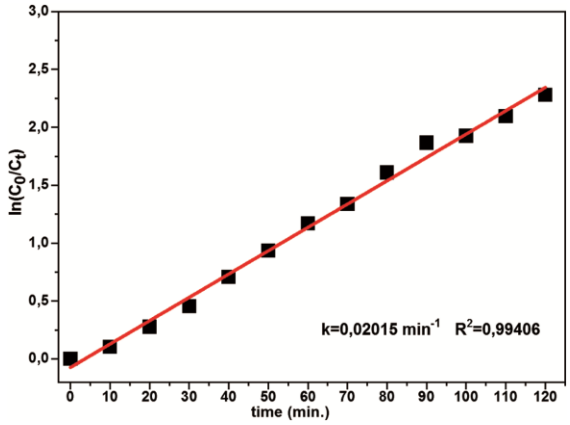

Fig. 12 — The plot of $\ln(C_0/C_t)$ against time of FeCrCoZrLa HEA.

value, which provides an idea about the photodegradation performance of the alloy sample, was found as k = 0.02015 min^{-1}. The obtained R^2 value is also very high which imply that the L–H model is very suitable for photocatalytic degradation of methylene blue dye.

4 Conclusions

In summary, equiatomic FeCrCoZrLa powder high entropy alloy has been successfully synthesized in nanostructure by mechanical alloying. The solid solution phase transformed into a BCC phase above 30 hours of milling. The nanostructure crystalline size of 15.44 nm was obtained after 50 h milling. The crystallographic structure of FeCrCoZrLa high entropy alloy calculated mixing enthalpy -10.97 J/mol, the mixing entropy 13.38 J/mol.K, average valence electron concentration (VEC) 6.6 and The atomic size difference (δ) 2.84. The DTA curves showed the stable structure of the 50-h milled FeCrCoZrLa HEA alloy powder for between 400 °C - 1000 °C. The photocatalytic degradation of the nanostructured alloy on MB was evaluated and as a result of this experiment it was found that the synthesized alloy has efficient photocatalytic activity. The photocatalytic test of rare earth element containing FeCrCoZrLa high entropy alloy on the MB photodegradation results in 89.76% degradation after 120 minutes. The synthesized nanostructured alloy exhibits highly effective photocatalytic properties on MB dyestuff, is promising in the treatment of organically polluted wastewater.

Acknowledgements

This work was supported by Kahramanmaraş İstiklal University, Scientific Research Projects Coordination Department, under Project No. 2021/3-4 BAP.

References

1 Yeh J W, Chen S K, Lin S J, Gan J Y, Chin T S, Shun T T, Tsau C H & Chang S Y, *Adv Eng Mater*, 6 (2004) 299.
2 Ren B, Liu Z X, Li D M, Shi L, Cai B & Wang M X, *J Alloys Compd*, 493 (2010) 148
3 Chen C L & Suprianto, *Intermetallics*, 113 (2019) 106570.
4 Suprianto & Chen C L, *Mater Sci Eng A*, 807 (2021) 140810.
5 John R, Karati A, Joseph J, Fabijanic D & Murty B S, *J Alloys Compd*, 835 (2020) 155424.
6 Thangaraju S, Bouzy E, Hazotte A, Tariq N H, Naeem M, Hasan B A, Akhter J I & Siddique M, *J Alloys Compd*, 19 (2013) 1700095.
7 Shu C, Chen K, Yang H, Chen M & He X, *Phys B Condens Matter*, 571 (2019) 235.
8 Ye Y F, Wang Q, Lu J, Liu C T & Yang Y, *Mater Today*, 19 (2016) 349.
9 Eißmann N, Klöden B, Weißgärber T & Kieback B, *Powder Metall*, 60 (2017) 184.
10 Panigrahi M & Avar B, *J Mater Sci Mater Electron*, 32 (2021) 21124.
11 Suryanarayana C, *Prog Mater Sci*, 46 (2001) 1.
12 Suryanarayana C, *Mater Res Lett*, 10 (2022) 619.
13 Shahmir H, Mehranpour M S, Shams S A A, Lee C S & Langdon T G, *High Entropy Alloy Mater*, (2022).
14 Chu C L, Chen W P, Liu J C, Chen Q & Fu Z Q, *Rare Met*, 41 (2022) 2864.
15 Su Z & Zhang Y, *J Mater Eng Perform*, 30 (2022).
16 S N Chan and C H Hsueh, J Alloys Compd 894, 162401 (2022)
17 Sun Y P, Wang Z, Yang H J, Lan A D & Qiao J W, *J Alloys Compd*, 842 (2020) 155825.
18 Zheng Z, Wang S, Long J, Wang J & Zheng K, *Corros Sci*, 164 (2020) 108359.
19 Gao X, Liu T, Zhang X, Fang H, Qin G & Chen R, *J Alloys Compd*, 918 (2022) 165584.
20 Ji W, Fu Z, Wang W, Wang H, Zhang J, Wang Y & Zhang F, *J Alloys Compd*, 589 (2014) 61.
21 Průša F, Cabibbo M, Šenková A, Kučera V, Veselka Z, Školáková A, Vojtěch D, Cibulková J, & Čapek J, *J Alloys Compd*, 835 (2020).
22 Průša F, Šenková A, Kučera V, Čapek J & Vojtěch D, *Mater Sci Eng A*, 734 (2018) 341.
23 Tekin M, Polat G, Kalay Y E & Kotan H, *J Alloys Compd*, 887 (2021) 161363.
24 Xu Q, Chen D Z, Wang C R, Cao W C, Wang Q, Cuı H Z, Zhang S Y & Chen R R, *Trans Nonferrous Met Soc China*, 31 (2021) 512.
25 Wang C, Li T H, Liao Y C, Li C L, Jang J S C & Hsueh C H, *Mater Sci Eng A*, 764 (2019) 138192.
26 Lu S F, Ma L, Wang J, Du Y S, Li L, Zhao J T & Rao G H, *J Alloys Compd*, 874 (2021).
27 Li G R, Liu M, Wang H M, Zhang D, Tang F, Wang C W, Zhao Y T, Chen G & Kai X Z, *JOM*, 72 (2020) 2332.
28 Lv Z Y, Liu X J, Jia B, Wang H, Wu Y & Lu Z P, *Sci Rep*, 6 (2016) 1.
29 Yang D, Liu Y, Han T, Zhou F, Qu N, Liao M, Lai Z & Zhu J, *J Alloys Compd*, 918 (2022) 165562.
30 Parakh A, Vaidya M, Kumar N, Chetty R & Murty B S, *J Alloys Compd*, 863 (2021) 158056.

31 Liu X, Cheng H, Li Z, Wang H, Chang F, Wang W, Tang Q & Dai P, *Vacuum*, 165 (2019) 297
32 Kerli S, Kavgacı M, Soğuksu A K & Avar B, *Brazilian J Phys*, 52 (2022) 1.
33 Wang N, *Surf Interfaces*, 33 (2022) 102265.
34 Petrović S, Rožić L, Grbić B, Radić N, Cherkezova-Zheleva Z & Stojadinović S, *J Solid State Chem*, 297 (2021) 1.
35 Kerli S, Soğuksu A K & Kavgacl M, *Int J Mod Phys B*, 34 (2020) 1.
36 Kumar A, Mucalo M, Bolzoni L, Li Y, Kong F & Yang F, *Metals (Basel)*, 12 (2022).
37 Tian F, Varga L K, Chen N, Shen J & Vitos L, *Intermetallics*, 58 (2015) 1.
38 Miracle D B & Senkov O N, *Acta Mater*, 122 (2017) 448.
39 Guo S & Lıu C T, *Prog Nat Sci Mater Int*, 21 (2011) 433.
40 Xu X D, Guo S, Nieh T G, Liu C T, Hirata A & Chen M W, *Materialia*, 6 (2019).
41 Chen W, Fu Z, Fang S, Xiao H & Zhu D, *Mater Des*, 51 (2013) 854.
42 Sekhar R A, Samal S, Nayan N & Bakshi S R, *J Alloys Compd*, 787 (2019) 123.
43 Cardoso K R, Izaias B da S, Vieira L de S & Bepe A M, *Mater Sci Technol*, 36 (2020) 1861.
44 Yang Y, Ling C, Yang M, Yang L, Wang D, Peng S & Shuai C, *Int J Bioprint*, 8 (2022) 96.
45 Eskalen H, Uruş S, Yaykaşlı H & Gögebakan M, *Alloy Mater Their Allied Appl*, 91 (2020).
46 Maulik O & Kumar V, *Mater Charact*, 110 (2015) 116.
47 Mishra R K & Shahi R, *J Alloys Compd*, 821 (2020) 153534.